Quaternary Geochronology 6 (2011) 295–303

Contents lists available at ScienceDirect

Quaternary Geochronology

journal homepage: www.elsevier.com/locate/quageo

Research Paper

Exposure dating of precariously balanced rocks

Greg Balco [a,*,1], Matthew D. Purvance [b,c,1], Dylan H. Rood [d,e,1]

[a] Berkeley Geochronology Center, 2455 Ridge Road, Berkeley, CA 94709, USA
[b] Seismological Laboratory, University of Nevada-Reno, Reno, NV 89557, USA
[c] Itasca Consulting Group, Minneapolis, MN 55401, USA
[d] Center for Accelerator Mass Spectrometry, Lawrence Livermore National Laboratory, Livermore, CA, USA
[e] Earth Research Institute, University of California, Santa Barbara, CA 93106, USA

ARTICLE INFO

Article history:
Received 19 April 2010
Received in revised form
16 March 2011
Accepted 24 March 2011
Available online 31 March 2011

Keywords:
Precariously balanced rocks
Paleoseismology
Cosmogenic-nuclides
Exposure dating
Beryllium-10

ABSTRACT

Precariously balanced rocks (PBRs) are freestanding boulders that are precarious or fragile in the sense that they could be toppled by relatively low-amplitude earthquake ground motion. They are important in paleoseismology because their continued existence limits the amplitude of ground motion experienced at their location during their lifetime. In order to make quantitative use of PBRs for seismic hazard studies, one must determine when they attained their present state of fragility, that is, the point in time when the contact between the rocks and the pedestals on which they rest was exhumed from surrounding soil and the rock became vulnerable to earthquake ground motions. Cosmogenic-nuclide exposure dating can be used for this purpose, but is complicated because nuclide production occurs throughout exhumation of the PBR, so the apparent exposure age of any part of the rock surface exceeds the time that the rock has actually been precariously balanced. Here we describe a method for determining the length of time that a PBR has been fragile by measuring cosmogenic-nuclide concentrations at several locations on the PBR surface, and linking them together with a forward model that accounts for nuclide production before, during, and after exhumation of the PBR. Fitting model to data yields the rate and timing of rock exhumation and thus the length of time the rock has been fragile. We use this method to show that an example PBR in southern California has been fragile for 18.7 ± 2.8 ka.

1. Precariously balanced rocks

As pointed out by Shaler (1896) and numerous subsequent researchers, delicate or fragile geologic features are important in paleoseismology because they would not survive significant ground motions, so the fact that they are still present limits the amplitude of shaking during their lifetime. These features include, among others, balanced rocks, rock stacks or piles, precipitous cliffs, arches, hoodos, and some speleothems. In this paper we are concerned with precariously balanced rocks (PBRs), which are a class of these features that consist of a single freestanding boulder resting on a stone pedestal in such a way that it could be toppled by relatively low amplitude earthquake ground motions (e.g., Brune, 1996). Subsequently we use the term 'fragile' to describe this condition. Specifically, fragility is the overturning potential as a function of ground motion amplitude, and one advantage of PBRs over other fragile features is that one can quantitatively determine their fragility by numerical calculations as well as field and laboratory experiments (Anooshehpoor et al., 2004; Purvance et al., 2008a).

In order to make quantitative use of PBR fragilities in seismic hazard studies, one must determine when the PBRs formed. By 'formation' of a PBR we mean the time when the freestanding boulder and its pedestal became free from surrounding regolith, thus making it possible for the boulder to shift and perhaps topple in an earthquake. Brune (1996) identified numerous PBRs in southern California and pointed out that their existence appeared inconsistent with existing seismic hazard estimates, but could only estimate when they formed by noting that the presence of rock varnish suggested at least thousands of years of exposure. Subsequently, Bell et al. (1998) attempted to estimate the formation age of some of these PBRs by rock varnish microstratigraphy and ^{36}Cl exposure dating. Correlation of rock varnish microlaminations to climate records yielded minimum exposure ages of 10,500–14,500 years for at least some parts of the rock surfaces, and apparent ^{36}Cl exposure ages from a single sample associated with each PBR were 13,000–73,000 years. Purvance et al. (2008b) assumed, based on these observations, that similar boulders in southern California had been fragile for at least 10,000 years, and combined this assumption with measurements of their fragilities to show

* Corresponding author. Tel.: +1 510 644 9200; fax: +1 510 644 9201.
E-mail address: balcs@bgc.org (G. Balco).
[1] Authors contributed equally. Listed in alphabetical order.

1871-1014/$ – see front matter © 2011 Elsevier B.V. All rights reserved.
doi:10.1016/j.quageo.2011.03.007

quantitatively that the existence of these PBRs was inconsistent with the 2002 USGS National Seismic Hazard Maps.

Measurements of PBR fragility could be used more effectively for seismic hazard studies if the formation age of the PBRs could be more precisely determined. Although the rock varnish microstratigraphy provides clear minimum ages for the surface exposure time of some parts of the PBRs, single apparent cosmogenic-nuclide exposure ages yield little information about the time the PBRs became fragile, because of several complications. The most important complication is that, as discussed below, these PBRs formed by exhumation from beneath a regolith layer. Because some cosmogenic-nuclide production occurs below the surface, cosmogenic nuclides begin to accumulate well before any part of a PBR is actually exhumed. Also, if a PBR was exhumed slowly, many parts of its surface could have been exposed at the surface for a long time before the rock actually became fragile. An additional complication is that typical PBRs are 1–2 m in size, a dimension similar to the characteristic attenuation length for cosmic rays at the Earth's surface. As the PBR becomes exposed, it acts to partially obstruct the cosmic ray flux at most locations on the surface of the PBR or its pedestal, and this shielding effect changes over time as the soil surface lowers. In this paper we deal with both of these complications by developing a quantitative model that predicts cosmogenic-nuclide concentrations at any point on the surface of a PBR as a function of its exhumation history. Given several measurements of cosmogenic-nuclide concentrations at varying heights on the surface of the PBR and its pedestal, one can find an exhumation history that best fits the measurements, and thus determine the formation age of the PBR. We then use this method to date an example PBR from southern California using measurements of cosmogenic ^{10}Be.

2. Forward model for cosmogenic-nuclide production in a PBR

2.1. Model setup

Precariously balanced rocks in desert areas of southern California, such as our example boulder discussed below (Fig. 1), are characteristic of regions where rounded granite boulders are formed below the ground surface by weathering along joint surfaces, and are subsequently exhumed by stripping of the surrounding regolith (Twidale, 1982; Oberlander, 1972). Thus, these PBRs are corestones formed below the surface and exposed to the cosmic-ray flux by gradual exhumation from beneath a regolith blanket (Fig. 2). As a result we require a model expression that describes changes in the concentration of a cosmogenic-nuclide during and after this process. We will write this expression for the nuclide we will use in a subsequent example, ^{10}Be in quartz, but it applies to any cosmogenic nuclide formed primarily by spallation and to a relatively small extent by muon interactions. The model resembles that used by Heimsath et al. (2000) to describe cosmogenic-nuclide accumulation in bedrock tors emerging from a soil-mantled landscape; the chief differences are that i) we account for production by muons as well as spallation; ii) we use analytical rather than numerical solutions to the differential equation governing nuclide accumulation; and iii) we account for partial shielding of the samples by the emerging PBR.

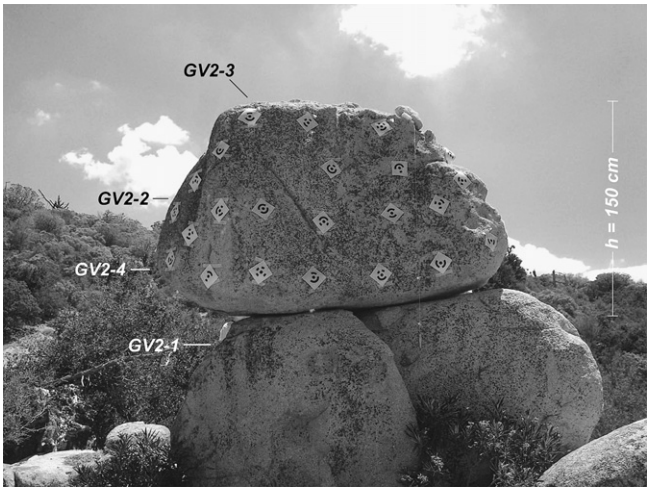

Fig. 1. Precariously balanced rock "GV2" at Grass Valley, CA. Labels show sample locations.

The model has four unknown parameters for which we will find optimal values by fitting model to data: $\epsilon_{0,sp}$ and $\epsilon_{0,\mu}$, which are used to describe the depth-nuclide concentration profile prior to PBR emergence (cm a^{-1}; see additional discussion below); t_0, the time that the uppermost point on the PBR became exposed (years before present); and ϵ_1, the lowering rate of the soil surface during PBR exhumation (cm a^{-1}). Given optimal values of these parameters we can compute the time t_{tip} (years before present) at which the contact points between the PBR and the pedestal become exposed, so that the rock becomes fragile: $t_{tip} = t_0 - h/\epsilon_1$, where h is the height of the PBR (cm).

2.1.1. Cosmogenic-nuclide concentrations prior to PBR exhumation

We are describing ^{10}Be concentrations in a number of samples collected from the surface of the PBR or pedestal at various heights; z_i is the vertical distance (cm) that sample i lies below the top of the PBR. First, we need to describe the height-nuclide concentration profile at time t_0. At this time, the entire PBR lies below the ground surface, so this is equivalent to describing the depth-nuclide concentration profile below an eroding surface. If we only consider spallogenic production, this depth-concentration profile is given by Lal (1988):

$$N_{10,0,sp} = \frac{P_{10,sp} e^{-z\rho/\Lambda_{sp}}}{\lambda_{10} + \epsilon_{0,sp}\rho/\Lambda_{sp}} \quad (1)$$

where $N_{10,0,sp}$ is the ^{10}Be concentration due to spallogenic production at time t_0, z is the depth below the surface (cm), λ_{10} is the ^{10}Be decay constant (4.99×10^{-7} a^{-1}), Λ_{sp} is the effective attenuation length for spallogenic production (160 g cm^{-2} for consistency with the shielding calculation described below; see discussion in Gosse and Phillips, 2001), and ρ is the rock density (g cm^{-3}). Note that by using a single value of ρ we are assuming that the PBR and the rock fragments and/or regolith that surrounded it in the past have the same density. As no information exists regarding the density of no-longer-extant material, this seems to be the most sensible approach. $P_{10,sp}$ is the surface ^{10}Be production rate due to spallation (atoms g^{-1} a^{-1}); in the subsequent example we estimate $P_{10,sp}$ using the scaling scheme of Stone (2000) as implemented in Balco et al. (2008), and the global calibration data set of Balco et al. (2008).

If the erosion rate had been steady for an extended period of time prior to t_0, that is, long enough for several attenuation lengths Λ_{sp} to have been removed, then $\epsilon_{0,sp}$ would be the erosion rate (cm yr^{-1}). This scenario is very restrictive and, in fact, it is most likely that the presence of PBRs implies an unsteady erosion rate: a long period of slow erosion and corestone formation followed by a period of rapid stripping of saprolite and exposure of the corestones. Thus, we cannot assume that erosion has been steady prior to t_0. If erosion is unsteady, Eq. (1) remains an accurate description of the subsurface nuclide concentrations due to spallation, except

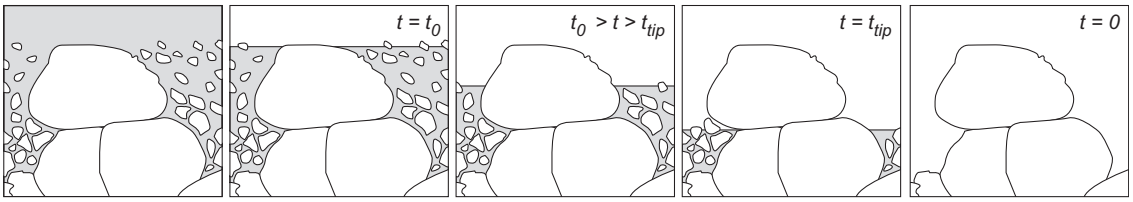

Fig. 2. Relationship of model time to PBR exhumation history. The PBR forms below the surface and is exposed by stripping of the surrounding regolith. At time t_0 the top of the PBR is exposed. At t_{tip} the bottom of the PBR is exposed and the rock is free to topple.

that $\epsilon_{0,sp}$ no longer corresponds to the instantaneous erosion rate at time t_0 (or at any other time for that matter). In this case $\epsilon_{0,sp}$ could be characterized as an *apparent* erosion rate, but is not the *actual* erosion rate. In other words, if the erosion rate changes, the nuclide concentration at any depth gradually changes in such a way as to approach equilibrium with the new erosion rate, but the functional form of the depth-nuclide concentration profile does not change. Bierman and Steig (1996) and Schaller et al. (2002) discuss this issue at length. The point of this discussion is that we can describe the depth-concentration profile for a particular production pathway at time t_0 in terms of a single parameter that has units of erosion rate (cm yr^{-1}), but we cannot interpret the best-fitting value of that parameter as the actual erosion rate at t_0 without making the unrealistic assumption of steady erosion.

In addition to the nuclide concentration-depth profile due to spallation at time t_0, we also need to account for the depth-nuclide concentration profile due to production by muons. This can be represented as a sum of several exponential functions that correspond to Eq. (1), as follows:

$$N_{10,0,\mu} = \sum_{j=1}^{3} \frac{P_{10,j} e^{-z\rho/\Lambda_j}}{\lambda_{10} + \epsilon_{0,\mu}\rho/\Lambda_j} \tag{2}$$

The parameters $P_{10,j}$ (atoms g^{-1} a^{-1}) and Λ_j (g cm^{-2}) that describe production due to muons are site-specific. We computed them as follows: first, we calculated the ^{10}Be production rate at the site due to muons as a function of depth, $P_{10,\mu}(z)$ (atoms g^{-1} a^{-1}) using a MATLAB implementation, described in Balco et al. (2008), of the method of Heisinger et al. (2002b,a). To obtain the $P_{10,j}$ and Λ_j we then fit these results with a simplified expression:

$$P_{10,\mu}(z) = \sum_{j=1}^{3} P_{10,j} e^{-z\rho/\Lambda_j} \tag{3}$$

Again, if the erosion rate was steady for an extended time prior to t_0, then $\epsilon_{0,\mu}$ would be equal to the actual erosion rate at t_0, which would further imply that $\epsilon_{0,\mu} = \epsilon_{0,sp}$. However, this is not true for unsteady erosion. The rate at which the nuclide concentration attributable to a particular production pathway reaches a new equilibrium value after a change in the erosion rate depends on the attenuation length associated with that pathway: longer attenuation lengths imply slower equilibration. This means that if we cannot assume steady erosion, we cannot assume that $\epsilon_{0,\mu} = \epsilon_{0,sp}$. Strictly, in fact, we would require three separate values of ϵ for each of the exponential terms in Eq. (2); here we make the approximation that due to i) the long integration time implied by the large attenuation length of production due to muons, and ii) the fact that the nuclide concentration due to production by muons is a small fraction of the total nuclide concentration, the single value $\epsilon_{0,\mu}$ is adequate to describe the nuclide concentration due to production by muons.

To summarize, even if we do not make any assumptions about the surface erosion history prior to t_0, we can parameterize the depth-nuclide concentration profile at t_0 in terms of two *apparent* erosion rates $\epsilon_{0,sp}$ and $\epsilon_{0,\mu}$. However, the best-fitting values of these parameters will not necessarily correspond to the actual erosion rate at t_0. In fact, they are unlikely to correspond to the actual erosion rate at any time. In addition, these parameters are not required to compute t_{tip}, so in the model fitting exercise below we will consider them nuisance parameters. Thus, the ^{10}Be concentration in quartz in sample i at t_0 is $N_{10,0,i}$ (atoms g^{-1}) such that:

$$N_{10,0,i} = \frac{P_{10,sp} e^{-z_i\rho/\Lambda_{sp}}}{\lambda_{10} + \epsilon_{0,sp}\rho/\Lambda_{sp}} + \sum_{j=1}^{3} \frac{P_{10,j} e^{-z_i\rho/\Lambda_j}}{\lambda_{10} + \epsilon_{0,\mu}\rho/\Lambda_j} \tag{4}$$

2.1.2. Cosmogenic-nuclide production during sample exhumation

We next consider nuclide production in sample i between the time the top of the PBR is exhumed (t_0) and the time the sample is exhumed. This reflects the rate ϵ_1 at which the soil surface drops during PBR exhumation, and the duration of this period of time is z_i/ϵ_1. The nuclide concentration developed in sample i during this time period is $N_{10,1,i}$ (atoms g^{-1}):

$$N_{10,1,i} = \int_0^{z_i/\epsilon_1} P_{10,sp}\, S_i(t\epsilon_1) e^{-\lambda_{10} t} dt + \sum_{j=1}^{3} \frac{P_{10,j}}{\lambda_{10} + \frac{\epsilon_1\rho}{\Lambda_j}} \left[1 - e^{-(\lambda_{10} + \frac{\epsilon_1\rho}{\Lambda_j})(\frac{z_i}{\epsilon_1})} \right] \tag{5}$$

Here the function $S_i(z)$ is a sample-specific function describing the fast neutron shielding factor at the site of sample i as a function of depth below the soil surface (dimensionless; the shielding factor is the ratio of the production rate at the shielded location to that at a point on an infinite, unobstructed flat surface). As discussed in the next section, once the top of the PBR breaks the surface, the PBR itself partially shields samples on the side of the PBR or on the pedestal. In this case the shielding geometry becomes quite complicated and must be computed numerically. Because of the much greater penetration depth of muons than of fast neutrons, we have ignored this effect in computing production by muons. As we discuss in detail in the next section, we found that we could approximate the numerical estimates of $S_i(z)$ by:

$$S_i(z) = S_{0,i} e^{-z\rho/L_i} \tag{6}$$

where $S_{0,i}$ (dimensionless) and L_i (g cm^{-2}) are sample-specific constants. With this approximation,

$$N_{10,1,i} = \frac{P_{10,sp} S_{0,i}}{\lambda_{10} + \frac{\epsilon_1\rho}{L_i}} \left[1 - e^{-\left(\lambda_{10} + \frac{\epsilon_1\rho}{L_i}\right)\left(\frac{z_i}{\epsilon_1}\right)} \right] + \sum_{j=1}^{3} \frac{P_{10,j}}{\lambda_{10} + \frac{\epsilon_1\rho}{\Lambda_j}} \left[1 - e^{-\left(\lambda_{10} + \frac{\epsilon_1\rho}{\Lambda_j}\right)\left(\frac{z_i}{\epsilon_1}\right)} \right] \tag{7}$$

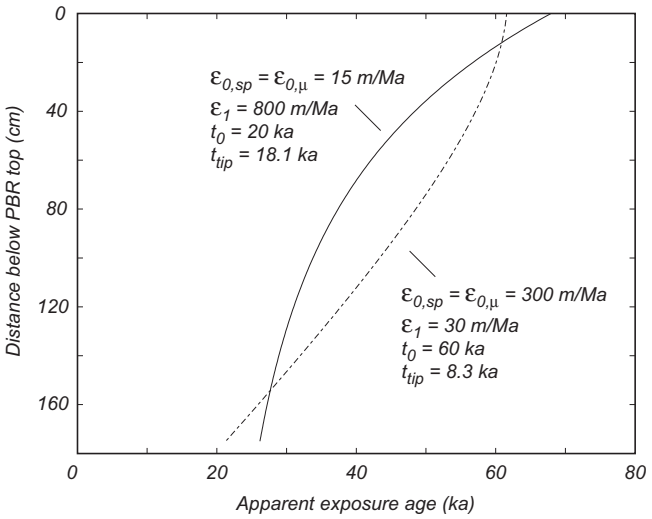

Fig. 3. Example height-nuclide concentration profiles for various exhumation histories. The model profiles are drawn for the location and elevation of the GV2 PBR, for a hypothetical 150-cm-high PBR that has equal geometric shielding at all heights. The *x*-axis is apparent exposure age, which is the nuclide concentration divided by the surface production rate. Rapid erosion prior to PBR exhumation, followed by slow exhumation of the PBR, produces a convex profile (dashed line). Slow erosion before exhumation, followed by rapid exhumation, produces a concave profile (solid line). The important point is that although these two scenarios produce similar nuclide concentrations (in fact, they are identical at two levels), they imply very different ages for the time the PBR became free to topple. Thus, one must measure nuclide concentrations in many samples from a range of elevations to characterize the shape of this profile and thus determine the tipping age of the PBR.

2.1.3. Cosmogenic-nuclide production after sample exhumation

We next consider nuclide production after sample i has been exhumed. The duration of this period is $t_0 - z_i/\epsilon_1$. The nuclide concentration developed in sample i during this time $N_{10,2,i}$ (atoms g^{-1}) is:

$$N_{10,2,i} = \frac{P_{10,sp}S_{0,i}}{\lambda_{10} + \frac{\epsilon_{s,i}\rho}{\Lambda_{sp}}}\left[1 - e^{-\left(\lambda_{10}+\frac{\epsilon_{s,i}\rho}{\Lambda_{sp}}\right)\left(t_0-\frac{z_i}{\epsilon_1}\right)}\right] + \sum_{j=1}^{3}\frac{P_{10,j}}{\lambda_{10}}\left[1 - e^{-(\lambda_{10})\left(t_0-\frac{z_i}{\epsilon_1}\right)}\right] \quad (8)$$

Here $\epsilon_{s,i}$ is the erosion rate of the PBR surface at sample i after it is exposed. We do not solve for this, so we must estimate it from other evidence, and we allow for the possibility that it may differ among the samples. Note that we ignore the effect of surface erosion on the nuclide concentration due to muons. In addition, Λ_{sp} is strictly the effective attenuation length for spallogenic production under an infinite flat surface, so this expression is somewhat oversimplified for samples that lie on the sides of the PBR. These simplifications are unimportant as long as the surface erosion rate is relatively slow, on the order of a few cm during the time the PBR has been exposed.

2.1.4. Total cosmogenic-nuclide concentration at the present time

The ^{10}Be concentration in sample i at the present time $N_{10,i}$ (atoms g^{-1}) is the sum of these contributions, adjusted for radioactive decay:

$$N_{10,i} = N_{10,0,i}e^{-t_0\lambda_{10}} + N_{10,1,i}e^{-(t_0-z_i/\epsilon_1)\lambda_{10}} + N_{10,2,i} \quad (9)$$

Fig. 3 shows example height-nuclide concentration profiles predicted by Eq. (9) for two contrasting exhumation scenarios. These emphasize two important points. First, the apparent exposure age of any part of the PBR (the apparent exposure age is the exposure age calculated on the basis of a single period of exposure at the present production rate) can be wildly in excess of the age that the PBR actually became fragile. Second, for any particular sample location (in fact, for two sample locations simultaneously), very different exhumation histories can yield identical nuclide concentrations. Thus, to determine the actual exhumation history, one must collect a number of samples over enough of a height range to adequately characterize the height–concentration profile.

2.2. Attenuation of the cosmic-ray flux by the PBR

This section describes how we obtained the parameters $S_{0,i}$ and L_i that describe the shielding of each sample by the PBR during various stages of exhumation. First, we developed a three-dimensional shape model for the PBR and pedestal using a photogrammetric method. We marked a number of points on the PBR and photographed it from multiple directions (Fig. 1). We then used the software package PhotoModeler (http://www.photomodeler.com) to identify common points in multiple photographs and photogrammetrically determine the relative positions of the camera positions and these common points. This process results in a set of three-dimensional (relative) coordinates for points lying on the PBR and pedestal surfaces. As PBRs mostly have convex shapes, we used the surface triangulation capability of PhotoModeler to fit a convex hull to points lying on the PBR and each pedestal block. This results in a representation of the PBR and each pedestal block as a closed, convex surface consisting of numerous triangular facets (Fig. 4). An estimate of the accuracy of this method is provided by Anooshehpoor et al. (2007), who used it to estimate the volume of test rocks that could subsequently be weighed; they found that estimated and measured rock volumes differed by a few percent or less. Although this accuracy estimate is not precisely applicable to the shielding calculation here, it shows that uncertainty in the PBR shape model is most likely minor in comparison to other uncertainties in the shielding calculation.

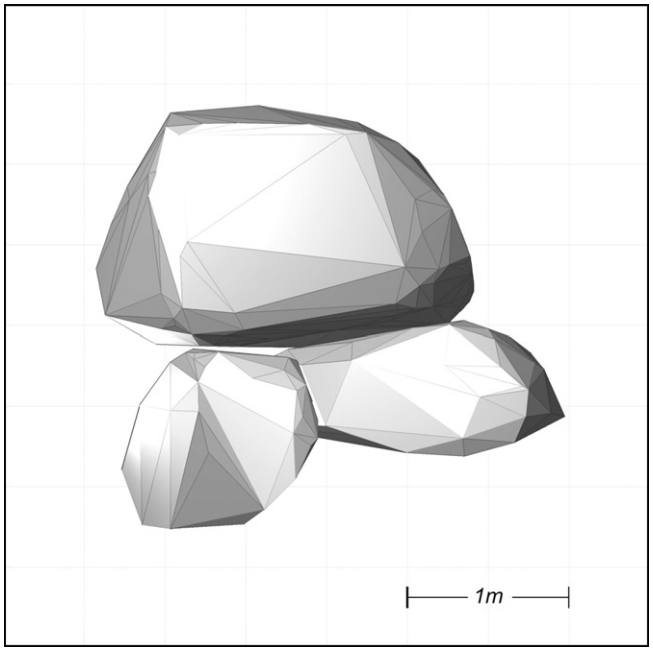

Fig. 4. The shape model of the GV2 PBR and pedestal blocks used in the shielding calculations. The view is the same as in Fig. 1.

We located the samples in the same coordinate system as the shape model using the same photogrammetric software. For each sample location, we calculated the shielding factor S (dimensionless) using a Monte Carlo integration, as follows.

First, we represented the cosmic-ray flux at the sample location by a series of rays, with randomly generated azimuth ϕ and horizon angle θ, terminating at the sample site. Values of ϕ are uniformly distributed between 0 and 2π, and values of θ are distributed between 0 and $\pi/2$, with probability of given θ proportional to $\sin^{2.3}\theta$ (see discussion of the angular distribution of the cosmic-ray flux in Gosse and Phillips, 2001). For each (ϕ, θ) pair, we determined whether a ray with that orientation intersected the PBR or pedestal before arriving at the sample location. In order to take account of sample thickness in this procedure, we defined the sample locations to be the center of the sample that was actually collected, somewhat interior to the surface of the PBR. Thus, all rays pass through at least some part of the PBR or pedestal. We calculated the total length of each ray l (cm) that lay within the PBR or pedestal, and computed an attenuation factor s (dimensionless) for that ray according to $s = \exp(-l\rho/\Lambda_p)$ where Λ_p is 208 g cm^{-2} (see Gosse and Phillips (2001) for discussion. This value for Λ_p corresponds to a value for Λ_{sp} of 160 g cm^{-2}). The shielding factor S for that sample location is then the average value of s over all iterations. We found that approximately 1000 iterations were required to converge on a reproducible value for S. To build up the function $S_i(z)$ required to evaluate Eq. (5), we repeated this calculation with the regolith surface defined to be at various heights above the sample location (Fig. 5). In this situation, rays terminating at the sample location experience attenuation by both regolith and rock. As discussed above, we assumed that regolith and rock have the same density. Fig. 6 shows that $S_i(z)$ conforms to Eq. (6) for all samples on the GV2 PBR. This is also true for all other PBRs we have investigated up to this point.

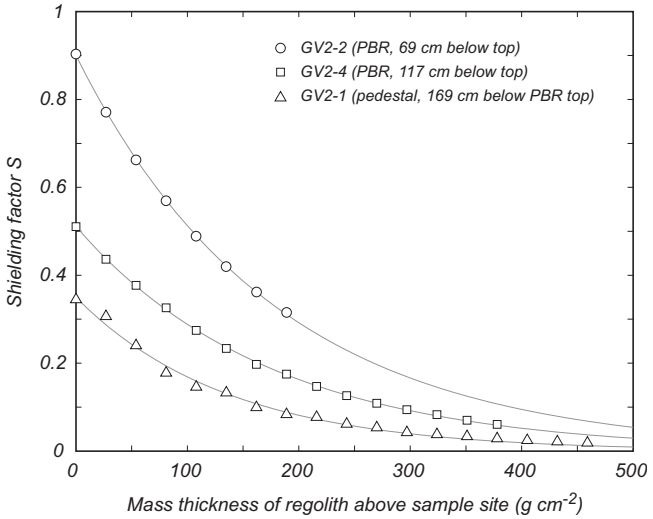

Fig. 6. Exponential fits to numerical calculations of the shielding factor for samples below the PBR top as a function of soil depth above the sample location. The symbols are the results of the Monte Carlo integration; the lines are given by Eq. (6) with the parameters from Table 1.

2.3. Model fitting

We fit the model to the measured nuclide concentrations by finding values of the free parameters $\epsilon_{0,sp}$, $\epsilon_{0,mu}$, ϵ_1, and t_0 that minimized the chi-squared misfit M between observed and predicted nuclide concentrations:

$$M = \sum_{i=1}^{n} \left[\frac{N_{10,i} - N_{10,m,i}}{\sigma N_{10,m,i}} \right]^2 \quad (10)$$

where $N_{10,m,i}$ is the measured ^{10}Be concentration in sample i (atoms g^{-1}), $\sigma N_{10,m,i}$ is its one-standard-error uncertainty (atoms g^{-1}), and n is the number of samples. As all of the sample locations are exposed at the present time, the parameters are subject to the constraint that the total amount of exhumation $t_0\epsilon_1$ must be greater than the distance that the lowest sample lies below the PBR top (note also that if this constraint is not met, Eqs. (7) and (8) will yield unphysical results for some samples). In addition, for better computational efficiency we limited the exhumation rate ϵ_1 to be less than 10 cm a^{-1}. Any exhumation rate higher than this can equivalently be considered instantaneous exhumation relative to PBR exposure ages of thousands to tens of thousands of years.

We cannot show analytically that this objective function and constraints always yield a unique minimum. The objective function is not convex. However, we explored this issue for the example data described below by randomly varying the starting guess over a large range of parameter space; we found that the optimization scheme always converged on a single minimum.

2.4. Potential weaknesses in this model

First, the assumption in this model that is most likely to fail in some natural cases is that the entire PBR is exhumed steadily at a fixed exhumation rate ϵ_1. Note that this assumption applies only to the time period during which all the samples are exhumed: the

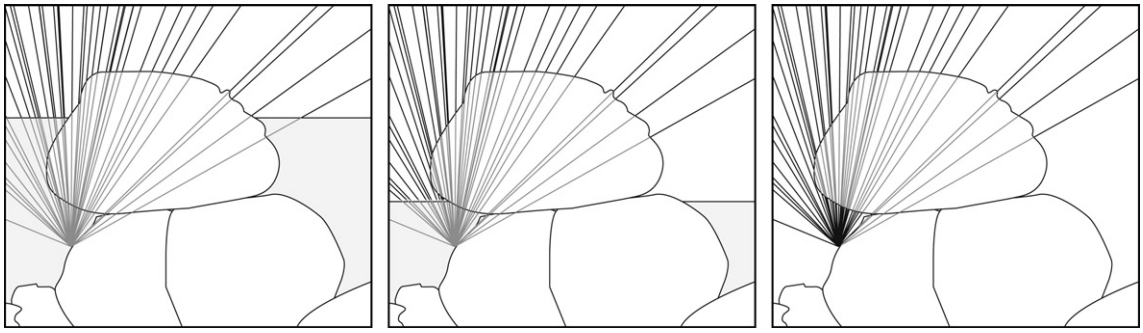

Fig. 5. Shielding effect of PBR and regolith cover on the cosmic ray flux at a representative sample location. The dark lines denote model cosmic-ray trajectories terminating at the sample location; the lightened parts of the lines highlight the portion of these trajectories that pass through rock or regolith. Before the sample location is exhumed (left panels), both the PBR and the remaining regolith act to attenuate the cosmic-ray flux; no trajectories reach the sample location directly. After the sample location is exhumed (right panel), some of the trajectories reach the sample location directly and others must pass through the PBR.

model contains no assumptions about the exhumation rate before the highest sample is exhumed or after the lowest sample is exhumed. We show later that the model does a good job of fitting measured nuclide concentrations from an example PBR, but it is likely that many PBRs emerge in multiple pulses of rapid exhumation separated by periods of relative stability. In this case the model might not fit measured nuclide concentrations. If one were to allow for unsteady exhumation, many more parameters would be required to describe nuclide accumulation during exhumation, and the problem would resemble the problem of identifying multiple earthquake slip events from a cosmogenic-nuclide profile on a fault scarp that has been addressed by, among others, Mitchell et al. (2001) and Benedetti et al. (2002).

Second, the model assumes that the orientation of the PBR was the same before exhumation that it is at present. Thus, our approach would fail if the PBR had tipped or rolled into its present orientation as it was exhumed. This issue can most likely be dealt within the process of selecting PBRs by carefully looking at their geometry and rock fabric orientation before attempting to date them.

A third potential weakness is that in some cases fitting the model to data relies heavily on the accuracy of nuclide production rates by muons. When the erosion rate prior to PBR exhumation is relatively slow, the two processes of i) production by muons prior to the start of PBR exhumation, and ii) production by all processes after all samples have been exhumed, both tend to flatten the nuclide concentration-height profile and thus have somewhat offsetting effects. Resolving these two similar effects requires an accurate representation of the relative importance of production by spallation and muons. Production rates due to muons are less well established than production rates due to spallation at present, which may lead to unrecognized systematic errors. A related issue is that, as discussed above, we have represented production due to muons by a sum of several exponentials with different attenuation lengths, but parameterized the nuclide concentration due to muons prior to PBR exhumation by a single apparent erosion rate. This may be oversimplified for some situations.

Finally, resolving nuclide inventories produced by spallation and muon interactions also depends on the accuracy of the shielding calculations. The calculations described above accurately implement the assumption that all cosmic-ray particles of interest come from outside the immediate region and their interactions with rock can be characterized by a single attenuation coefficient, but this assumption explicitly disregards the energy distribution of cosmic rays as well as any secondary particle production and escape. This could potentially lead to unrecognized systematic errors in the calculated values for $S_{0,i}$ and L_i. At present it is not clear how important these effects are.

3. An example from Grass Valley, southern California

3.1. The Grass Valley PBR

The "GV2" PBR shown in Fig. 1 is located in the central San Bernardino Mountains (SBM) of southern California, specifically within the Big Bear block of the SBM between the Santa Ana and North Frontal thrust faults of the San Andreas fault system. The SBM consist of crystalline basement rocks including Precambrian gneiss and schist intruded by two generations of Mesozoic granitic plutons (Barth, 1990). The GV2 PBR itself is granite. The geomorphology of the SBM is characterized by a high-elevation, low-relief plateau, covered by deeply weathered granite saprolite, that is in places deeply incised by river canyons. The low-relief plateau is believed to have been formed by Miocene weathering prior to uplift of the mountain block (Oberlander, 1972). Stratigraphic evidence shows that uplift postdated the Miocene and may have been as recent as 2–3 Ma (Blyth et al., 2000; Spotila et al., 1998). This uplift event presumably initiated river canyon incision which has since then been propagating headward into the low-relief interior of the range. Binnie et al. (2007) found that apparent basin-scale erosion rates for watersheds within the high-elevation, low-relief plateau are 50–130 m Ma^{-1}. The GV2 site lies within this low-relief, high-elevation zone, within a small (ca. 1 km^2) watershed whose lower reaches are littered with PBRs and loose granite boulders, but whose upper reaches remain covered by regolith and saprolite and display few boulders. An abrupt steepening of the channel slope separates these two zones. This geomorphic arrangement suggests that time-transgressive stripping of regolith and saprolite, presumably at the leading edge of headward-propagating incision into the central parts of the range, is currently proceeding upward from the bottom of the watershed. The GV2 PBR is located in the lower bouldery zone, adjacent to a dry wash that forms the central drainage of the watershed.

Table 1
^{10}Be concentrations and sample-specific constants for samples on the GV2 PBR.

Sample name	Distance below PBR top z_i (cm)	Sample thickness (cm)	[^{10}Be][a] (10^3 atoms g^{-1})	$S_{0,i}$	L_i (g cm^{-2})	Assumed $\epsilon_{s,i}$ (cm a^{-1})
GV2-3	0	4.5	688 ± 16	0.96	160	2×10^{-4}
GV2-2	69	4	410.3 ± 6.7	0.90	179	0
GV2-4	117	3.5	207.6 ± 4.4	0.51	174	0
GV2-1	169	5	163.3 ± 3.8	0.33	142	0

[a] Normalized to the isotope ratio standards of (Nishiizumi et al. (2007)).

Much of the surface of GV2 is covered with rock varnish. We did not investigate rock varnish microstratigraphy at this site. However, studies of varnish microstratigraphy at other sites in Southern California with similar climate implied that no surface erosion had taken place for 10,000–15,000 years (Bell et al., 1998). The summit of the PBR is not varnished and has a corrugated surface with ~2–3 cm of relief, indicating some surface erosion. Thus, we assumed $\epsilon_s = 0$ for samples from the varnished sides of the PBR and pedestal, and $\epsilon_s = 2 \times 10^{-4}$ cm a^{-1} for the uppermost sample (Table 1).

3.2. ^{10}Be measurements

We collected three samples from the GV2 PBR, at the top surface and at two locations on the sides, and one sample from the pedestal (Fig. 1). We crushed and sieved rock samples to extract the 0.25–0.5 mm size fraction and separated and purified quartz by selective etching in HF. We then added a carrier solution derived from deep-mined beryl with a ^{10}Be/^{9}Be ratio of $2 \pm 2 \times 10^{-16}$, dissolved the quartz, extracted Be by SiF_4 evaporation and column chromatography, and measured the Be isotope ratio by accelerator mass spectrometry (AMS). We carried out both chemical preparation and AMS analysis at the Center for Accelerator Mass Spectrometry, Lawrence Livermore National Laboratory. Rood et al. (2010) describe the AMS measurement procedure. Total carrier and process blanks were 33,000 ± 15,000 atoms, 0.2–1.5% of the total number of atoms measured in each sample. Table 1 and Fig. 7 show the ^{10}Be concentrations.

3.3. Results, discussion, and conclusions

We used the 'fmincon' function of the MATLAB Optimization Toolbox to fit model to measurements. Tables 1 and 2 show the values of all the site-specific and sample-specific constants needed to evaluate the model equations. The best-fitting values for the free

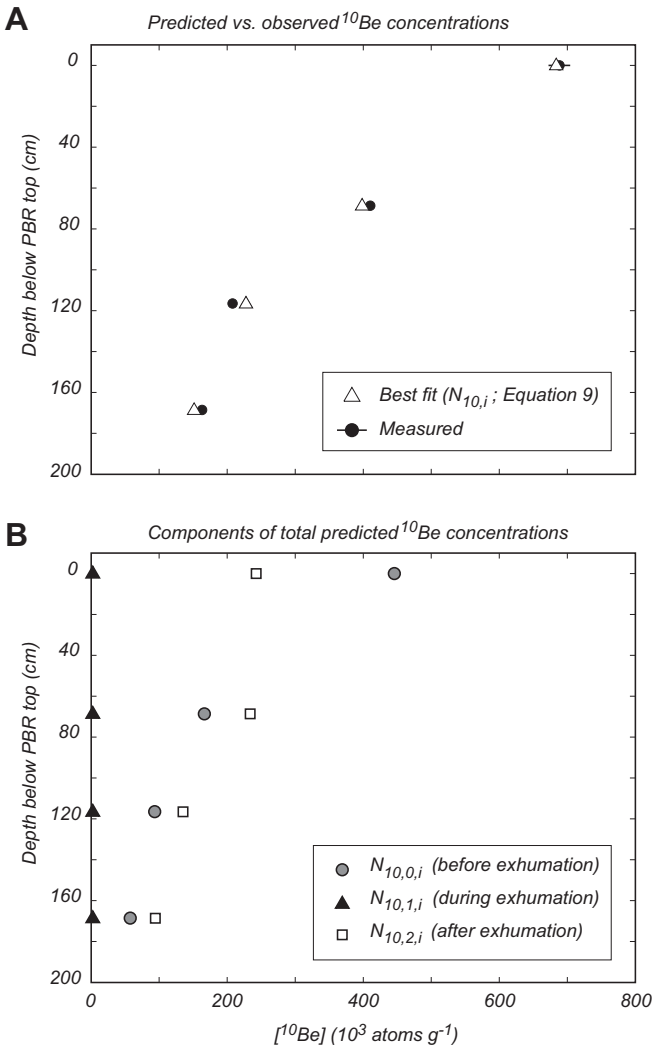

Fig. 7. Measured nuclide concentrations in GV2 samples compared with those predicted by the forward model and best-fitting parameters. Upper panel A shows measured ^{10}Be concentrations compared with those predicted by the forward model (Eq. (9)) and best-fitting parameters. Error bars show 1σ uncertainty on measured nuclide concentrations; error bars that are not visible are equal to or smaller than the size of the symbols. Lower panel B shows components of the total predicted nuclide concentration attributable to various phases of PBR exhumation, from Eqs. (4), (5), and (8).

parameters are $\epsilon_{0,sp} = 1.8 \times 10^{-3}$ cm a^{-1}, $\epsilon_{0,\mu} = 2.0 \times 10^{-3}$ cm a^{-1}, $\epsilon_1 = 10$ cm a^{-1}, and $t_0 = 18.8$ ka. These results imply $t_{tip} = 18.7$ ka. As noted above, the optimal value of ϵ_1 is the maximum value we allowed in the optimization, that is, the best-fitting parameters imply essentially instantaneous exhumation within years to decades. This exhumation rate is much faster than apparent basin-scale erosion rates in this region. However, as noted above, the PBR is located adjacent to a channel that is locally incising into saprolite and regolith. As channel erosion in arid landscapes such as this one is commonly episodic and associated with large flood events, it is likely that the channel could incise 2–3 m vertically and/or laterally within a series of floods over several years. Thus, there is no conflict between the conclusion that this particular PBR was exhumed rapidly and the observation that apparent basin-scale erosion rates in the region are relatively low.

Fig. 7 shows the fit of model to data. It is clear that the model closely duplicates the main features of the data, but the best-fitting parameters yield a value for the misfit statistic M of 42, which is much higher than expected if scatter of the data around the best-fitting model prediction is due to measurement uncertainty alone. However, one cannot interpret this value as a statistical significance level for two reasons. First, we have four free parameters and four observations, so there are no degrees of freedom. Second, and more importantly, in computing M we have not accounted for any of the systematic uncertainties that could arise from i) assumptions in the shielding calculations (see discussion above) or ii) the assumption that the exhumation rate was steady throughout exhumation of the PBR. Errors from these sources are likely, but difficult to quantify. Overall, because of the success of the model in reproducing the main features of the data set, we conclude that the model most likely adequately fits the data, but we do not have a basis for calculating the degree of confidence in this conclusion.

Table 2
Site-specific constants for the GV2 PBR.

Latitude	34.2788°N
Longitude	117.2471°W
Elevation (m)	1510
Rock density ρ (g cm^{-3})	2.67
$P_{10,sp}$ (atoms g^{-1} a^{-1})	12.5[a]
$P_{10,1}$ (atoms g^{-1} a^{-1})	0.014
$P_{10,2}$ (atoms g^{-1} a^{-1})	0.20
$P_{10,3}$ (atoms g^{-1} a^{-1})	0.075
Λ_1 (g cm^{-2})	128
Λ_2 (g cm^{-2})	1010
Λ_3 (g cm^{-2})	2171

[a] Normalized to the isotope ratio standards of Nishiizumi et al. (2007).

Estimating the uncertainty in the best-fitting value of t_{tip} is also difficult for the same reasons. First, we estimated this uncertainty by a Monte Carlo simulation in which we varied the measured nuclide concentrations by independently sampling the $N_{10,m,i}$ from normal distributions with mean and standard deviation given by the values in Table 1. Fig. 8 shows the results. This yields an internal uncertainty (i.e., including measurement uncertainties only) of 2.1 ka. Including the production rate uncertainty from Balco et al. (2008) yields a total (or external) uncertainty of ±2.8 ka. Another method for estimating confidence intervals for parameter estimates in a model-fitting exercise of this sort is to infer them from the relationship of the chi-squared misfit to the parameter values, as described in Bevington and Robinson (1992) among others. With zero degrees of freedom, however, this is not possible. The

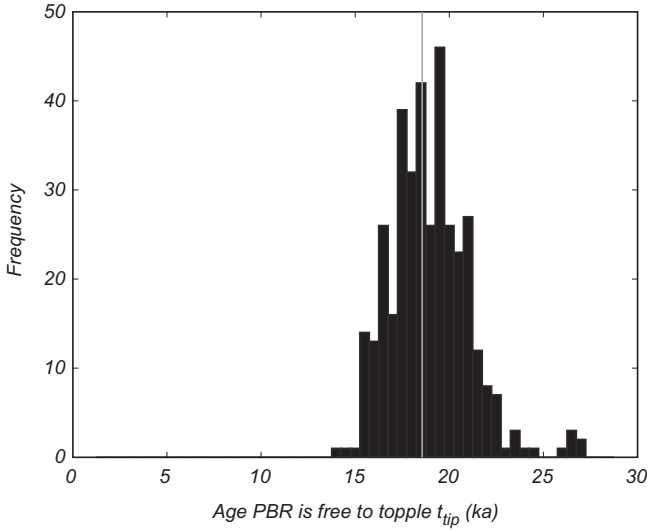

Fig. 8. Results of a 400-point Monte Carlo uncertainty analysis, including measurement uncertainties only, for the age the GV2 PBR became free to topple (t_{tip}). The grey line shows the best-fitting value (18,700 years).

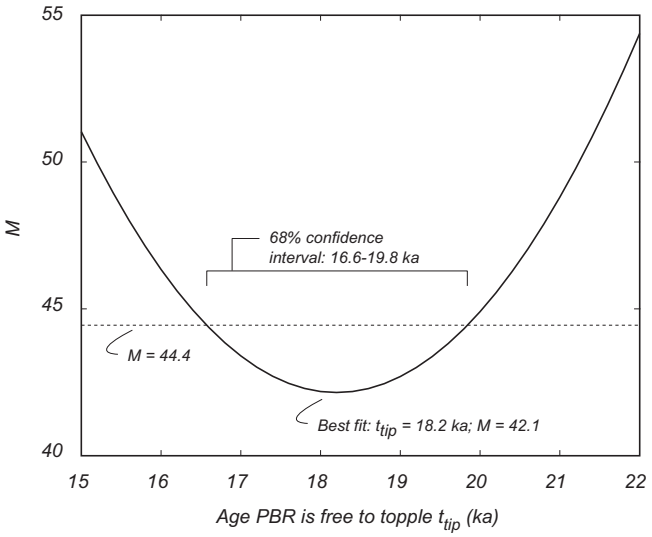

Fig. 9. Confidence interval estimate for t_{tip} obtained from the relationship of the chi-squared misfit statistic M to the value of t_{tip} for the simplified 2-parameter optimization (see text for explanation).

preferred solution to this problem would be to collect additional samples from the PBR so that the number of measurements exceeded the number of free parameters; this would also help to evaluate the uncertainty stemming from the steady-exhumation assumption. Alternatively, a reviewer of this paper, Dr. Ángel Rodés, pointed out that in our example the fact that the best-fitting parameters imply rapid exhumation of the PBR means that one could fix the value of ϵ_1 at 10 cm yr^{-1}, reducing the number of free parameters to three and providing one degree of freedom. This is correct, and in addition, the fact that in this example the best-fitting values of $\epsilon_{0,sp}$ and $\epsilon_{0,\mu}$ are similar means that one could also set $\epsilon_{0,sp} = \epsilon_{0,\mu}$, further reducing the number of free parameters to two. This strategy would unacceptably reduce the generality of the model for other PBRs, but would allow an uncertainty estimate for this particular one. These simplifications slightly change the best-fitting value of t_{tip} to 18.2 ka and yield a 68% confidence interval of 16.6–19.8 ka ($\pm$1.6 ka; this is the internal uncertainty; see Fig. 9), which is similar to the internal uncertainty derived from the Monte Carlo simulation.

This reviewer also pointed out that one could try to estimate the additional model uncertainty contributed by uncertainties in the shielding calculation (which we have not yet taken into account) by assuming that the uncertainties in the shielding factors $S_{0,i}$ are independent and normally distributed, and choosing a common uncertainty for these values that would yield a value of M near the expected value (1.4 for the 2-parameter case described above). For example, a fractional uncertainty in the shielding calculations of 0.2 (i.e., 20%) would yield a minimum value for M of 1.3 and a 68% confidence interval for t_{tip} of 14.4–31.2 ka. However, we view this approach as inappropriate because uncertainties in the sample-specific shielding factors are neither independent or normally distributed. They are not independent because the simplifying assumptions that we made in carrying out the shielding calculations would have similar effects on samples in similar geometric configurations, and they are not normally distributed because they stem from simplifying assumptions and not from measurements with normal uncertainty distributions.

Overall, we adopt the Monte Carlo uncertainty estimate as the most plausible given the available information, and we conclude that the GV2 PBR has been fragile for 18.7 $\pm$ 2.8 ka. The reliability of this uncertainty estimate could be improved by collecting and analyzing more samples at additional heights on the PBR.

Acknowledgements

This study could not have been carried out without the collaboration of many researchers who are part of a broader study of southern California PBRs, in particular Rasool Anooshehpoor, Jim Brune, Lisa Grant Ludwig, and Katherine Kendrick. In addition, MP thanks Lesley Perg for ideas and suggestions early in the project. Funding for this work was provided by Southern California Earthquake Center (SCEC) Award no. 10118 (to Lisa Grant Ludwig), a Lawrence Livermore National Laboratory Lawrence Scholar Program Fellowship (to DR), NSF Postdoctoral Fellowship Award no. EAR-0948350 (to DR), and by the Ann and Gordon Getty Foundation. Portions of this work were performed under the auspices of the US Department of Energy by Lawrence Livermore National Laboratory under Contract DE-AC52-07NA27344. SCEC is funded by NSF Cooperative Agreement EAR-0106924 and USGS Cooperative Agreement 02HQAG0008. This paper is SCEC Contribution 1480. We thank Drs. Régis Braucher and Ángel Rodés for comprehensive and helpful reviews.

Editorial handling by: D. Bourlès.

References

Anooshehpoor, A., Brune, J., Zeng, Y., 2004. Methodology for obtaining constraints on ground motion from precariously balanced rocks. Bulletin of the Seismological Society of America 94, 285–303.

Anooshehpoor, A., Purvance, M., Brune, J., Rennie, T., September 2007. Reduction in the uncertainties of the ground motion constraints by improved field-testing techniques of precariously balanced rocks. In: Proceedings of the 2007 Annual Southern California Earthquake Conference Meeting. Southern California Earthquake Conference, Palm Springs, CA, pp. 80–81.

Balco, G., Stone, J., Lifton, N., Dunai, T., 2008. A complete and easily accessible means of calculating surface exposure ages or erosion rates from ^{10}Be and ^{26}Al measurements. Quaternary Geochronology 3, 174–195.

Barth, A., 1990. Mid-crustal emplacement of Mesozoic plutons, San Gabriel Mountains, California, and implications for the geologic history of the San Gabriel terrane. In: Anderson, J. (Ed.), The Nature and Origin of Cordilleran Magmatism. Geological Society of America Memoir, Vol. 174. Geological Society of America, Boulder, CO, pp. 33–45.

Bell, J., Brune, J., Liu, T., Zreda, M., Yount, J., 1998. Dating precariously balanced rocks in seismically active parts of California and Nevada. Geology 26 (6), 495–498.

Benedetti, L., Finkel, R., Papanastassiou, D., King, G., Armijo, R., Ryerson, F., Farber, D., Flerit, F., 2002. Post-glacial slip history of the Sparta fault (Greece) determined by ^{36}Cl exposure dating: evidence for non-periodic earthquakes. Geophysical Research Letters 29, 1246.

Bevington, P., Robinson, D., 1992. Data Reduction and Error Analysis for the Physical Sciences. WCB McGraw-Hill.

Bierman, P., Steig, E., 1996. Estimating rates of denudation using cosmogenic isotope abundances in sediment. Earth Surface Processes and Landforms 21, 125–139.

Binnie, S., Phillips, W., Summerfield, M., Fifield, L., 2007. Tectonic uplift, threshold hillslopes, and denudation rates in a developing mountain range. Geology 35, 743–746.

Blyth, A., Burbank, D., Farley, K., Fielding, E., 2000. Structural and topographic evolution of the central Transverse Ranges, California, from apatite fission track, (U-Th)/He and digital elevation model analysis. Basin Research 12, 97–114.

Brune, J., 1996. Precariously balanced rocks and ground-motion maps for southern California. Seismological Society of America Bulletin 86, 43–54.

Gosse, J., Phillips, F., 2001. Terrestrial in situ cosmogenic nuclides: theory and application. Quaternary Science Reviews 20 (14), 1475–1560.

Heimsath, A., Chappell, J., Dietrich, W., Nishiizumi, K., Finkel, R., 2000. Soil production on a retreating escarpment in southeastern Australia. Geology 28 (9), 787–790.

Heisinger, B., Lal, D., Jull, A.J.T., Kubik, P., Ivy-Ochs, S., Knie, K., Nolte, E., 2002a. Production of selected cosmogenic radionuclides by muons: 2. Capture of negative muons. Earth and Planetary Science Letters 200 (3–4), 357–369.

Heisinger, B., Lal, D., Jull, A.J.T., Kubik, P., Ivy-Ochs, S., Neumaier, S., Knie, K., Lazarev, V., Nolte, E., 2002b. Production of selected cosmogenic radionuclides by muons 1. Fast muons. Earth and Planetary Science Letters 200 (3–4), 345–355.

Lal, D., 1988. In situ produced cosmogenic isotopes in terrestrial rocks. Annual Reviews of Earth and Planetary Science 16, 355–388.

Mitchell, S., Matmon, A., Bierman, P., Enzel, Y., Caffee, M., Rizzo, D., 2001. Displacement history of a limestone normal fault scarp, northern Israel, from cosmogenic ^{36}Cl. Journal of Geophysical Research 106 (B3), 4247–4264.

Nishiizumi, K., Imamura, M., Caffee, M., Southon, J., Finkel, R., McAnich, J., 2007. Absolute calibration of ^{10}Be AMS standards. Nuclear Instruments and Methods in Physics Research B 258, 403–413.

Oberlander, T., 1972. Morphogenesis of granite boulder slopes in the Mojave Desert, California. Journal of Geology 80, 1–20.

Purvance, M., Anooshehpoor, A., Brune, J., 2008a. Freestanding block overturning fragilities: numerical simulation and experimental validation. Earthquake Engineering and Structural Dynamics 37, 791–808.

Purvance, M., Brune, J., Abrahamson, N., Anderson, J., 2008b. Consistency of precariously balanced rocks with probabilistic seismic hazard estimates in southern California. Bulletin of the Seismological Society of America 98, 2629–2640.

Rood, D., Hall, S., Guilderson, T., Finkel, R., Brown, T., 2010. Challenges and opportunities in high-precision Be-10 measurements at CAMS. Nuclear Instruments and Methods in Physics Research B 268, 730–732.

Schaller, M., von Blanckenburg, F., Veldkamp, A., Tebbens, L., Hovius, N., Kubik, P., 2002. A 30 000 yr record of erosion rates from cosmogenic ^{10}Be in Middle European river terraces. Earth and Planetary Science Letters 204, 307–320.

Shaler, N., 1896. Aspects of the Earth. Charles Scribner's Sons, New York.

Spotila, J., Farley, K., Sieh, K., 1998. Uplift and erosion of the San Bernardino Mountains associated with transpression along the San Andreas fault, California, as constrained by radiogenic helium thermochronology. Tectonics 17, 360–378.

Stone, J.O., 2000. Air pressure and cosmogenic isotope production. Journal of Geophysical Research 105 (B10), 23753–23759.

Twidale, C., 1982. Granitic Landforms. Elsevier, Amsterdam.